Disponible en **www.hormigonyacero.com**
https://doi.org/10.33586/hya.2025.4147

# Fracture Monitoring in Encased Composite SFRC–Steel Beams Using DIC Under Static Loading

## *Monitorización mediante DIC del proceso de fractura de vigas mixtas de HRFA-acero estructural con perfiles embebidos bajo carga estática*

**Riccardo Zanon[a], Vaibhav W. Masih[b], Markus Schäfer[a], Sohanth T. Maganty[b], Ángel De La Rosa[c] & Gonzalo Ruiz[b,*]**

[a] *Department of Engineering, University of Luxembourg, 6 rue Richard Coudenhove-Kalergi, L-1359 Luxembourg.*
[b] *ETSI Caminos, C. y P., Universidad de Castilla-La Mancha, Av. Camilo José Cela s/n, 13071 Ciudad Real, Spain.*
[c] *DIMME, Grupo de Durabilidad e Integridad Mecánica de Materiales Estructurales, Universidad Rey Juan Carlos, C. Tulipán s/n, 28933 Móstoles, Madrid, Spain.*

**Recibido el 2 de septiembre de 2025; revisado el 4 de octubre de 2025, aceptado el 9 de noviembre de 2025**

## ABSTRACT

This study presents an experimental investigation into the crack initiation and propagation of full-scale load tests performed on encased composite steel-concrete beams, where the concrete is reinforced by conventional rebars together with high-strength steel fibers. Six beams were tested under three-point bending with quasi-static loading, including sagging and hogging configurations. One specimen from each configuration was subjected to various steps of sustained displacement to assess relaxation effects and observe time-dependent cracking phenomena. Full-field strain and crack evolution were monitored using a Digital Image Correlation (DIC) system alongside conventional instrumentation. The DIC system allowed high-resolution tracking of strain patterns, crack initiation and spacing, and crack mouth opening displacement at different load stages. These measurements were taken in a 660 mm wide region corresponding to the midspan. Results show that Steel Fiber-Reinforced Concrete (SFRC) was effective in controlling crack propagation and preventing concrete crushing in compression. At failure, sagging configurations exhibited several distributed cracks in the plastic hinge, and high ductility was achieved due to the favorable presence of the exposed steel flange on the tensile side. In hogging configurations, the steel profile was less effective in the tensile region, resulting in the formation of a dominant crack that concentrated damage at the ultimate state; however, these configurations also exhibited a ductile failure mode. Sustained loading did not significantly reduce the load-bearing capacity, although crack depth and opening did slightly increase. DIC proved effective in revealing strain redistribution and crack branching not captured by traditional sensors. The top SFRC layer of all the beams exhibited compressive strains of up to 1% without complete crushing or spalling, thus maintaining its functionality throughout the test. These findings confirm the validity of the compressive model for SFRC material outlined in Annex L of Eurocode 2, even for full-scale structures.

KEYWORDS: Encased composite SFRC--steel beams; DIC monitoring; crack width and spacing in composite structures; ductility of SFRC in compression.

## RESUMEN

Este estudio presenta una investigación experimental sobre la iniciación y propagación de fisuras en ensayos a escala real realizados sobre vigas mixtas acero-hormigón con perfiles embebidos, donde el hormigón está reforzado con armaduras convencionales y con fibras de acero de alta resistencia. Se ensayaron seis vigas mediante flexión en tres puntos con carga cuasiestática, incluyendo configuraciones de flector positivo y negativo. Una viga de cada configuración fue sometida a varias etapas de carga sostenida para evaluar efectos de relajación y observar fenómenos de fisuración dependientes del tiempo. La evolución completa de deformaciones y fisuras se monitorizó mediante un sistema de correlación digital de imágenes (DIC) junto con instrumentación convencional. El sistema DIC permitió un seguimiento de alta resolución de los patrones de deformación, la iniciación y espaciamiento de fisuras, y la apertura de la boca de las fisuras en diferentes etapas de carga. Estas mediciones se realizaron en una zona de 660 mm de ancho correspondiente al vano central. Los resultados muestran que el hormigón reforzado con fibras de acero (HRFA) fue eficaz en el control de la propagación de fisuras y en la prevención del fallo del hormigón en compresión. En el fallo, las configuraciones con momento positivo presentaron varias fisuras distribuidas en la rótula plástica, y se alcanzó una alta ductilidad gracias a la presencia beneficiosa del perfil de acero en la zona traccionada. En configuraciones con momento negativo, el perfil de acero fue menos eficiente en la región traccionada, lo que resultó en la formación de una fisura dominante que concentró el daño en el estado último; sin embargo, estas configuraciones también mostraron un modo de fallo dúctil. La carga sostenida no redujo significativamente la capacidad portante, aunque la profundidad y apertura de fisuras aumentaron ligeramente. El sistema DIC demostró ser eficaz para revelar redistribuciones de deformación y ramificaciones de fisuras no captadas por sensores tradicionales. La capa superior de HRFA en todas las vigas presentó deformaciones de compresión de hasta un 1% sin llegar a aplastamiento completo ni desprendimiento, manteniendo así su funcionalidad durante todo el ensayo. Estos hallazgos confirman la validez del modelo de compresión para el HRFA descrito en el Anexo L del Eurocódigo 2, incluso para estructuras a escala real.

PALABRAS CLAVE: Vigas compuestas encapsuladas de acero y hormigón reforzado con fibras de acero (SFRC); monitoreo mediante DIC; ancho y espaciamiento de fisuras en estructuras compuestas; ductilidad del SFRC a compresión.

---

* Persona de contacto / *Corresponding author*:
Correo-e / *e-mail*: gonzalo.ruiz@uclm.es (Gonzalo Ruiz)

How to cite this article: Zanon, R., Masih, V., Schäfer, M., Maganty, S., De la Rosa, Ángel, & Ruiz, G. (2026). Fracture Monitoring in Encased Composite SFRC--Steel Beams Using DIC Under Static Loading. *Hormigón y Acero*. 77(308):27-46. https://doi.org/10.33586/hya.2025.4147

## 1.
## INTRODUCTION

Steel–concrete composite systems are widely adopted in bridges, transfer girders, metro platforms, and high-rise structural cores due to their superior mechanical performance, fire resistance, and ductility. Fully encased configurations, where structural steel profiles are embedded within reinforced concrete, provide enhanced confinement and corrosion protection compared to concrete-filled tubes, leading to better performance under axial and flexural loading [1], [2], [3]. However, when high-strength concrete is employed in such encasement, it can introduce premature cover spalling and brittle failure modes [4], which compromise the ductility expected from composite interaction.

Steel Fiber-Reinforced Concrete (SFRC) has emerged as a promising alternative to traditional stirrups in composite members. The randomly distributed steel fibers bridge cracks and enhance tensile resistance, delay crack propagation, and improve post-peak load-bearing capacity [5], [6], [7], [8], [9]. These enhancements contribute significantly to both ultimate and serviceability limit states. The new Eurocode 2 Annex L (2022) officially includes constitutive models for SFRC in structural design [9], [10]. This update introduces residual strength-based compressive and tensile laws, which eliminate the need for traditional reinforcement under certain conditions, and allow for more efficient use of structural steel [8], [9].

Recent studies have confirmed the efficacy of SFRC in controlling crack widths, increasing energy absorption, and improving rebalancing of internal forces in coupon-scale elements [11]. Nonetheless, large-scale structural validation of these models, especially in beams with realistic reinforcement layouts and sustained loading conditions, remains limited. Understanding the fracture behavior at full scale is critical to confirming the applicability of Annex L provisions and to supporting SFRC-based design for high-performance infrastructure.

Steel fibers also enable the development of High-Technology Concrete (HTC), characterized by increased ductility, enhanced flexural strength, and superior strain hardening [9], [11]. HTC has been shown to delay localization and reduce early-age cracking. Its structural implementation, however, depends not only on material characterization but also on validating global and local responses under service-level actions such as relaxation and sustained loads. These conditions are typical of real structures but are rarely simulated in beam-scale experiments.

Traditional instrumentation, such as strain gauges and Linear Variable Differential Transformers (LVDTs), is limited to point-based measurements, lacking the spatial resolution needed to monitor early cracking, strain redistribution, or crack spacing [12]. In contrast, Digital Image Correlation (DIC) enables full-field strain tracking and crack opening measurement with sub-millimeter resolution.

DIC has been widely adopted in coupon-scale and small-component testing of concrete, composites, and fiber-reinforced systems, offering powerful tools for evaluating crack opening, strain localization, and fatigue progression [13], [14]. Recent reviews have emphasized its growing application to large-scale structures, though its deployment in full-scale SFRC–steel composite beams remains limited due to experimental complexity and data processing challenges [14], [15].

In this context, the present study presents a full-scale experimental campaign using DIC to monitor the fracture behavior of SFRC-encased steel composite beams subjected to both monotonic and sustained loading. Six beams were tested under three-point bending, in both sagging and hogging configurations, to explore flexural performance under varying strain gradients. One beam from each configuration was subjected to several steps of sustained loading to evaluate time-dependent crack propagation and strain relaxation.

A preliminary version of this study was presented in conference format, focusing on global load–displacement responses and structural capacity [16]. The present work expands significantly on that study by incorporating high-resolution DIC tracking, sustained loading regimes, and quantitative crack spacing and Crack Mouth Opening Displacement (CMOD) analysis. Through this integration, we aim to bridge the gap between SFRC material characterization and structural-scale validation for design.

The key contributions of this work are as follows:

- Full-field monitoring of strain localization and crack evolution in SFRC–steel composite beams using DIC.
- Evaluation of CMOD, crack spacing, and ductility metrics under both static and sustained loading.
- Comparative fracture analysis between sagging and hogging configurations, capturing the influence of steel profile position on crack distribution and strain behavior.
- Experimental validation of the compressive model for SFRC proposed in Annex L of Eurocode 2 using structural-scale data.

Crack spacing was analyzed both manually and through DIC in a 660 mm midspan zone. Crack evolution was correlated with load–displacement trends, and localized strain drops were linked to crushing, fiber bridging, and crack bifurcation. CMOD values at failure ranged from 10 to 42 mm, with hogging beams exhibiting more localized crack openings. The DIC system proved essential in capturing detailed crack evolution, especially during sustained load holds where subtle strain redistribution and crack branching occurred. Unlike LVDTs, DIC provided spatial resolution of crack opening along the full beam depth and helped differentiate between fiber-dominated ductile failure and localized concrete crushing.

This study contributes to performance-based design approaches for SFRC composite systems by demonstrating how fiber-reinforced HTC beams behave under realistic loading conditions. The findings directly inform the extension of Eurocode 2 Annex L provisions to full-scale applications and support the use of DIC as a viable fracture monitoring tool in future standardization efforts.

The remainder of this paper is organized as follows: Section 2 describes the beam configuration, reinforcement, and HTC mix design; it also outlines the experimental methods, including DIC instrumentation and sustained loading protocol. Section 3 presents the results of load–displacement response, strain evolution, CMOD, and crack spacing. Section 4 discusses the implications for SFRC design and Annex L validation. Section 5 summarizes the key findings and offers future research directions.

## 2.

## MATERIALS AND METHODOLOGY

### *2.1. Test Specimen Configuration*

The test specimens were designed as full-scale composite beams to represent filler beam decks commonly used in bridges. The cross-section geometry is compliant with filler beam decks covered by prEN 1994-2 [17]. Each specimen had a total length of 4400 mm and a constant rectangular cross-section measuring 650 mm in width and 330 mm in height, see Fig. 1.

The embedded steel profile used was a HEA260 made from S460M structural steel. It features a total flange width of 260 mm, an overall section depth of 250 mm, a flange thickness of 12.5 mm, and a web thickness of 7.5 mm. Tensile tests were conducted on both the web and the flange to determine their effective yield strength and rupture strength (see Table 2). Since all the beams tested were sourced from the same parent beam, the variation in material properties is

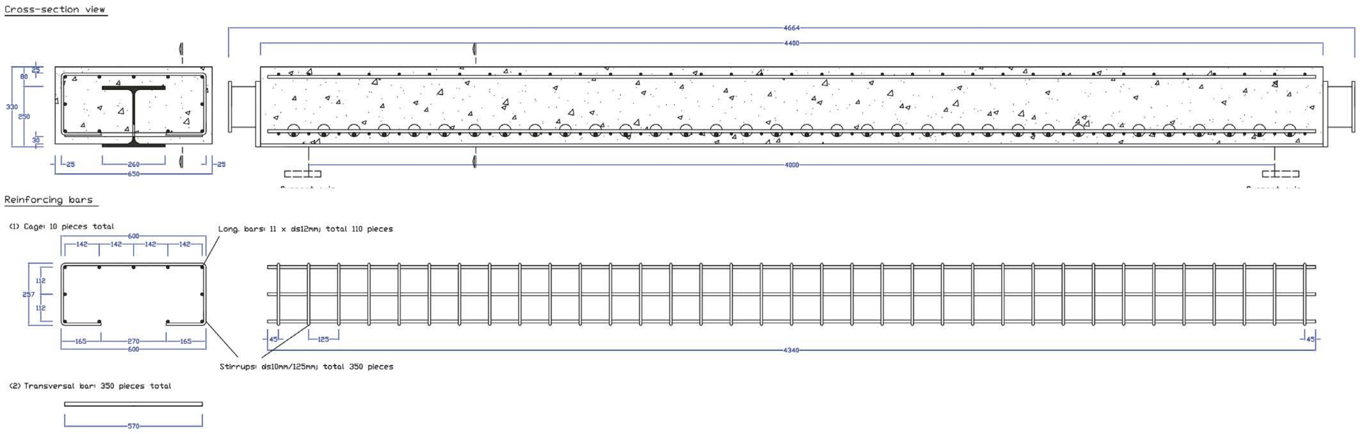

Figure 1. Cross and longitudinal section of the beam and reinforcement disposition.

minimal. The bottom flange is exposed and located beneath the concrete layer. Additionally, the concrete was reinforced with conventional reinforcement, which remained consistent along the entire length of the beam:

- 11 longitudinal rebars $d_s$ 12 mm arranged above and below the steel section,
- 10 mm stirrups placed at 125 mm intervals, closed at the bottom by overlapping a transverse bar led through the web in diameter 16 mm,
- A concrete cover of 25 mm on the top and sides and 30 mm at the bottom.

Tensile tests were conducted on the longitudinal rebars, which were all manufactured from the same wire rod in a single production batch. This resulted in reduced variability among the tests, with the standard deviation of five specimens being 7.2 MPa (equating to 1.1% of the yield strength) and 4.1 MPa (or 0.57% of the ultimate strength) for the respective strengths measured.

## 2.2. High-Technology Concrete

The concrete used in this study was a steel fiber-reinforced HTC mix, formulated to balance enhanced mechanical performance with practical casting and pumping conditions. The formulation follows the industrial methodology validated by De La Rosa et al. [11], [18] for both quasi-static and dynamic regimes.

The HTC mix consisted of Portland cement (CEM I 52.5 R-SR 5), mineral filler, fine and coarse limestone aggregates, water, and two admixtures: a polycarboxylate-based superplasticizer and an air-entraining agent. Hooked-end steel fibers HE++75/35 (35 mm long, 0.75 mm diameter) were included at a dosage of 47.1 kg/m3 (0.6% vol.). The full mix composition is shown in Table 1.

**TABLE 1.**
**Mix composition.**

| *Component* | *kg/m³* |
|---|---|
| Cement (CEM I 52.5 R-SR 5) | 380 |
| Fine aggregate (0/4 mm) | 950 |
| Coarse aggregate (4/12 mm) | 525 |
| Coarse aggregate (12/20 mm) | 225 |
| Limestone filler | 90 |
| Water | 182 |
| Superplasticizer | 3.8 |
| Air-entraining agent | 1.52 |
| Steel fibers (HE++75/35) | 47.1 |

All specimens were stored under ambient indoor conditions for 5–6 months prior to testing. Mechanical characterization at the time of testing yielded compressive strength $f_{cm}$=55.9 MPa, modulus of elasticity $E_c$=33.3 GPa, and Poisson's ratio $v$=0.21. Characteristic residual flexural strengths determined from prismatic specimens (750 × 150 × 150 mm$^3$) were: at CMOD 0.5 mm $f_{R,1k}$=2.9 MPa, and at CMOD 2.5 mm $f_{R,3k}$=2.6 MPa [16], [18].

A total of 6 beams were cast and tested under different loading conditions, including sagging, hogging, and sustained regimes. The beams were supported on elastomeric pads and tested using a three-point bending setup with a clear span of 4200 mm. Fig. 2 shows one of the beams during testing in hogging configuration, while Fig. 3 illustrates the sagging and hogging configurations.

**TABLE 2.**
**Steel material properties used in beam specimens.**

| *Component* | *Nominal Class* | *$R_{p0.2}$[MPa]* | *Rm [MPa]* |
|---|---|---|---|
| Structural steel | S460M | 480 | 612 |
| Longitudinal rebars | B500B | 624 | 720 |
| Steel fibers (HE++75/35) | — | 2150 | — |

**TABLE 3.**
**Mechanical properties of the steel fiber-reinforced concrete mix.**

| *Component* | *Class* | *$f_{cm}$ [MPa]* | *$E_{cm}$ [GPa]* | *$f_{R,1k}$ [MPa]* | *$f_{R,3k}$ [MPa]* |
|---|---|---|---|---|---|
| SFRC Mix | C45/55 – 2.5c | 55.9 | 33.3 | 2.9 | 2.6 |

## 2.3. Experimental Methods

### 2.3.1. Test Setup and Instrumentation

The experimental setup was designed to evaluate the fracture behavior of full-scale SFRC–steel composite beams under controlled static loading conditions. All beams were tested using a quasi-static three-point bending configuration with a clear span of 4200 mm, see Figs. 2 and 3. The primary objective of the setup was to capture the evolution of strain and crack patterns under both positive (sagging) and negative (hogging) bending moments using both conventional and full-field measurement techniques.

A servo-hydraulic actuator was used to apply vertical loads at midspan in displacement control mode. The initial displacement rate was 0.7 mm/min during the first hour, and later 2.5 mm/min to the end of the test. The actuator was connected to a high-capacity load cell to monitor real-time force application. To ensure accurate boundary conditions, the beams were supported on neoprene pads placed over steel rollers, enabling rotation and small horizontal displacements to simulate realistic support conditions (see Fig. 4).

LVDTs were strategically installed to record vertical displacements at several key locations along the beam span. A total of seven LVDTs were employed to capture global and local deflection profiles, midspan displacements, and differential deformations near the supports. The placement of these transducers is shown in Figure 4a and further detailed in Figure 5a.

Strain gauges (SGs) were affixed to both the concrete surface and the embedded steel-section to monitor longitudinal strains during loading. A total of 12 strain gauges were used per beam in the sagging configuration: six on the SFRC surface (top and bottom) and six on the steel flange/web to assess strain compatibility and stress redistribution between the composite materials. In the hogging setup, additional strain gauges were positioned to capture localized stress states near the compression zone, as seen in Figure 4b.

Complementing the conventional sensors, a 2D DIC system was installed to monitor the full-field strain distribution over a 660 mm zone centered at midspan the region of maximum bending moment. The DIC camera was mounted orthogonally to the beam surface and calibrated prior to testing. The speckle pattern required for DIC tracking was applied using a controlled screen-printing method [19] to ensure high contrast

Figure 2: Beam being tested in hogging configuration.

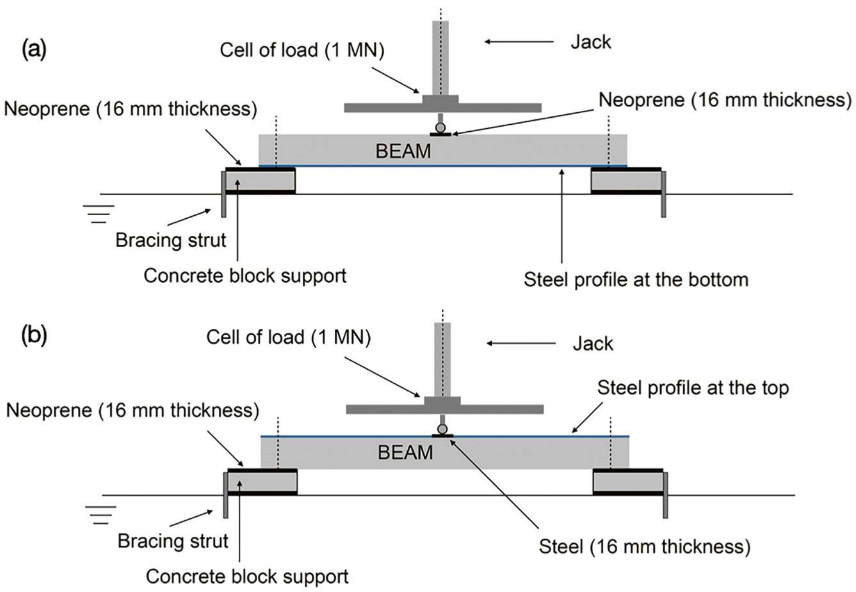

Figure 3. Experimental configurations for bending tests: (a) Sagging setup and (b) Hogging setup.

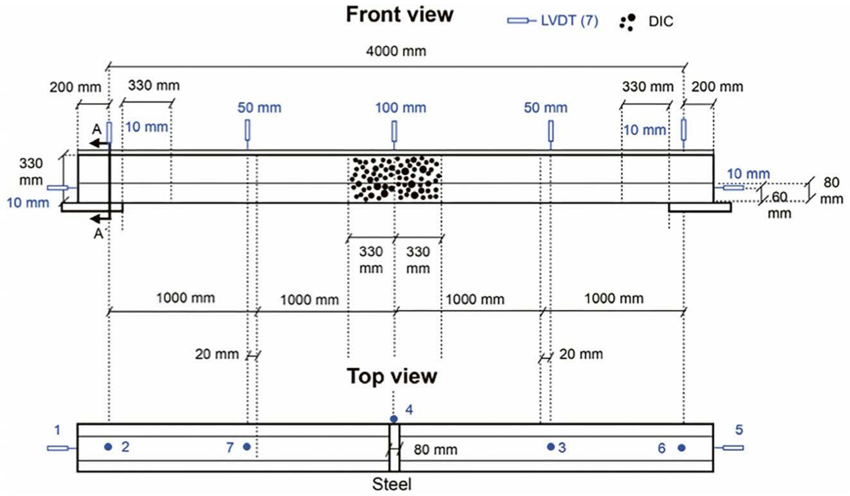

(a) Hogging setup: Locations of LVDTs (1–7), DIC region, and strain gauges (SGs 1–12) on the SFRC-steel composite beam under positive bending

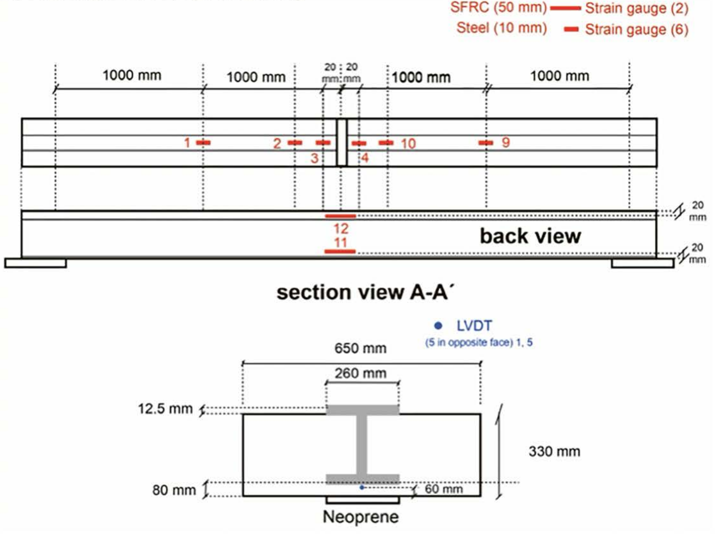

(b) Hogging setup: Instrumentation layout showing strain gauges on SFRC and steel plates, LVDTs on both sides, and section A–A' with neoprene support and steel section steel profile.

Figure 4. Experimental configurations for composite SFRC-steel beam tested under three-point bending: (a) Front and top views of the hogging setup showing LVDT locations, DIC region, and overall geometry of the SFRC, and (b) back and sectional views of the hogging setup showing strain gauge arrangement on SFRC and steel layers, and LVDT positioning at the supports.

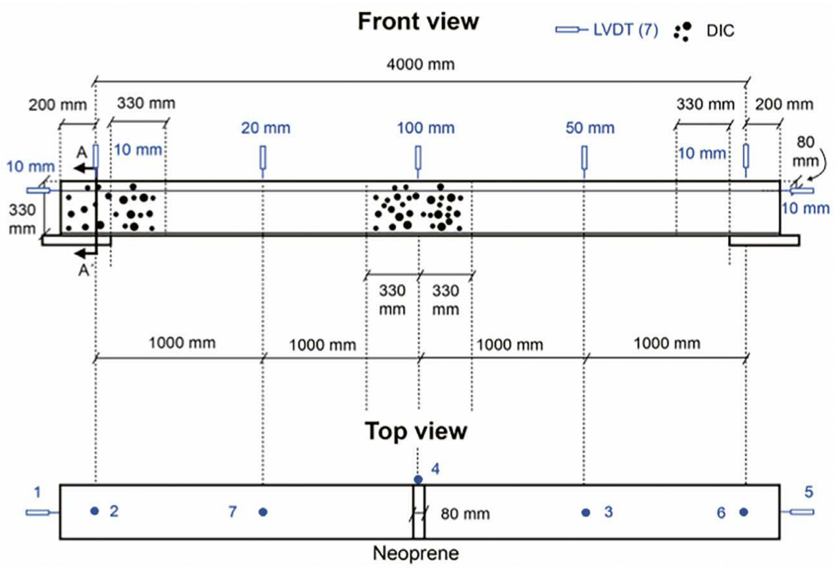

(a) Front and top views of the sagging setup showing LVDT locations, DIC region, and overall geometry of the SFRC–steel composite beam.

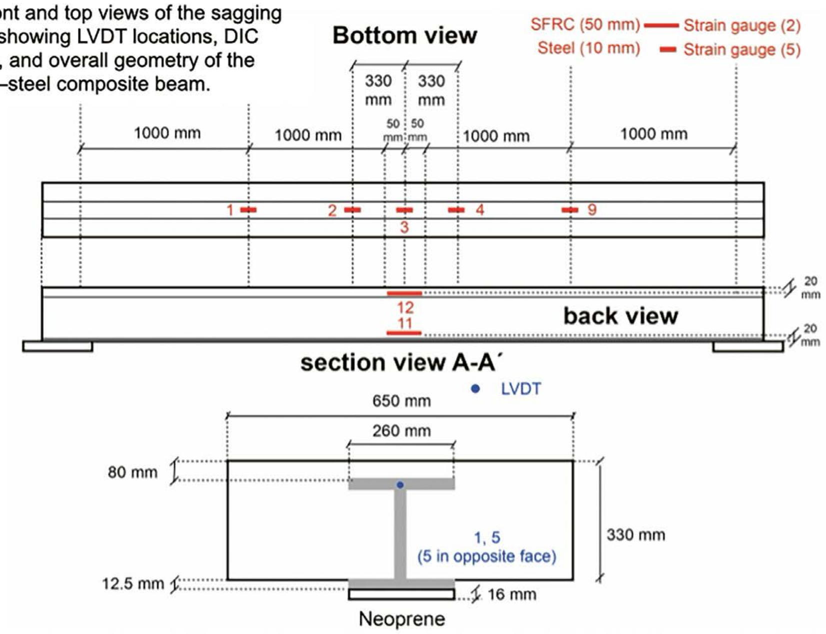

(b) Back and sectional views of the sagging setup showing strain gauge arrangement on SFRC and steel layers, and LVDT positioning at the supports.

Figure 5. Instrumentation and geometry of the sagging configuration used for three-point bending tests on SFRC-steel composite beams: (a) Front and top views with LVDTs and DIC region, and (b) back and sectional views detailing strain gauge layout and support conditions.

and spatial consistency (Fig. 7). A fine polyester screen mesh with a predefined circular-dot stencil was held flush against the concrete surface, and matte black acrylic ink was deposited through the open apertures using standard flood squeegee passes. This process produced uniform dots of approximately 3 mm diameter and consistent inter-dot spacing, effectively mitigating overspray and dot coalescence typical of freehand spraying. The controlled application improves gray-level distribution and correlation robustness in large-area DIC [20].

Instrumentation layout diagrams (Fig. 5a and 5b) illustrate both front and rear views of the sagging beam configuration, clearly identifying LVDT positions, strain gauge locations, and the DIC region of interest.

In two beams (Beams 3 and 6), a sustained load protocol was introduced. The test procedure began with an initial ramp-up, starting at a velocity of 0.5 mm/min over a period of 40 minutes, followed by a 20-minute pause. This sequence was repeated three times, totaling three hours. The purpose of these three initial ramps was to achieve approximately 40% of the peak load. After the initial ramps, a new ramp was introduced, increasing the velocity to 1 mm/min for 20 minutes, followed by a 15-minute pause. This was succeeded by another ramp at a speed of 2 mm/min for 20 minutes, which was followed by a 15-minute pause. Finally, the test concluded with a last ramp at 2 mm/min until the end of the procedure. In total, the duration of this relaxation test was 4 hours and 40 minutes. This allowed assessment of strain redistribution and the effect of sustained stress on crack evolution and depth.

This comprehensive instrumentation scheme enabled multi-scale monitoring of the beam response, ranging from

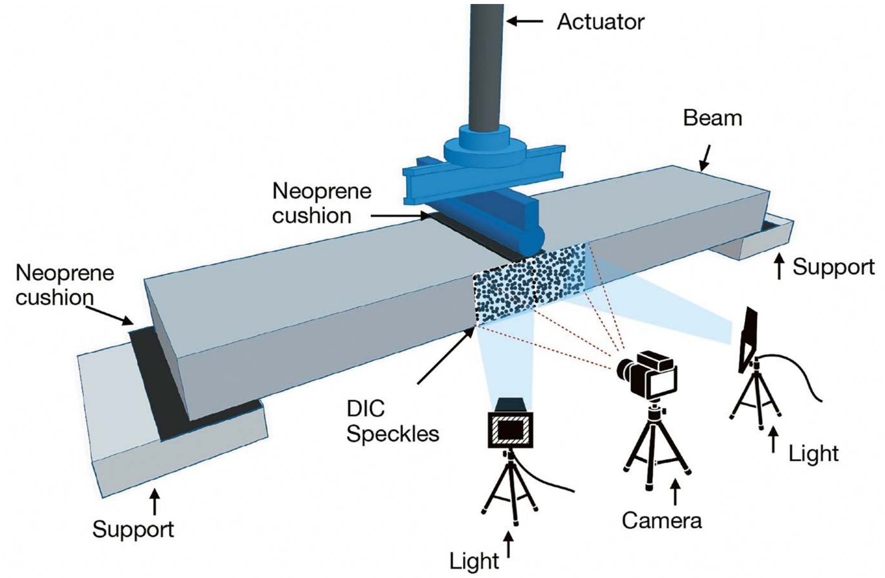

Figure 6. Setup of the components of the DIC system.

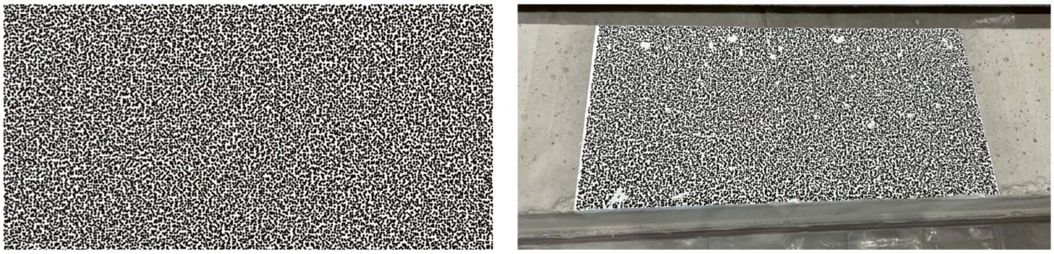

(a) Speckle pattern (3 mm, 85%–85%).

(b) Speckle application on the beam surface.

Figure 7. Final speckle pattern and its application to the beam surface.

point-based strain and displacement measurements to full-field DIC analysis. The setup provided high-fidelity data for validating SFRC constitutive models under both service and ultimate load conditions, contributing to the structural-scale verification of Eurocode 2 Annex L provisions.

### *2.3.2. Digital Image Correlation (DIC) Methodology*

A two-dimensional Digital Image Correlation (2D-DIC) system (ARAMIS Adjustable Base 2.3M) was used to capture full-field strain and displacement fields in the SFRC–steel composite beams during quasi-static and sustained loading. The system was deployed to monitor a 660 mm zone centered at midspan, which corresponds to the region of maximum flexural demand (see Fig. 6). This length was selected to match twice the beam depth, ensuring coverage of the expected crack formation zone.

The optical configuration employed a fixed industrial camera with a global shutter and a resolution of 1936 × 1216 pixels. A non-interchangeable lens, optimized for geometric stability, was used to provide consistent magnification and focus. Polarizing filters were installed on both the lens and illumination system to suppress glare and enhance speckle contrast. The camera was mounted perpendicular to the specimen surface using a rigid frame to avoid perspective distortion.

A speckle pattern consisting of 3 mm diameter black dots was applied to the concrete surface using the screen-printing technique described above. The pattern achieved approximately 85% coverage and 85% gray-level variation, which ensured high correlation quality during image post-processing. Several speckle designs were first trialed on a prototype wooden beam using the GOM live “pattern/correlation quality" check to compare performance [21]. The final pattern was selected based on stable facet tracking during preliminary sequences and a good calibration result (green indicator) after proper sensor warm-up and exposure setup. During testing, images were captured at defined load stages in 2D mode; the first image, taken at a preload of approximately 5 kN, served as the reference, and subsequent frames were correlated to obtain in-plane displacement and strain fields. Load-image synchronization was achieved via software time-stamps by ensuring synchronization between the timeline of the image captured and the progression of testing.

Image acquisition was performed at 1 Hz during quasi-static loading, and at 10 Hz during select 2-second bursts under sustained load conditions. These parameters provided a balance between temporal resolution and manageable data volume.

DIC analysis was conducted using the GOM Correlate software. A facet size of 35 × 40 pixels was used, defining the subset for displacement tracking. The strain fields obtained were processed using internal smoothing and filtering functions to enhance signal quality. The software’s tracking tools were also used to measure CMOD and to map crack spacing along the midspan region.

CMOD was extracted using the two-point distance tool by placing markers on opposite sides of the crack mouth. The relative displacement between these markers was recorded continuously, allowing for sub-pixel resolution of crack opening throughout the loading protocol. Crack spacing was evaluated by identifying crack tips on sequential displacement contour maps and computing inter-crack distances.

This non-contact optical method was cross-validated with conventional point-based instruments such as LVDTs and strain gauges. CMOD and displacement values recorded by DIC were compared with those from mechanical sensors to ensure consistency. The DIC method also captured data in regions where traditional instrumentation could not be installed, especially near fiber-bridging zones or in regions with complex cracking.

Overall, the DIC system provided a high-fidelity, full-field dataset that complemented traditional instrumentation and enabled advanced fracture analysis of the composite beams. It proved especially valuable for evaluating strain localization, crack propagation under sustained loads, and ductility indicators that are critical to validating SFRC constitutive models at structural scale.

## 3.
## RESULTS AND ANALYSIS

### *3.1. Load–displacement behavior*

Figure 8 presents the midspan load–displacement responses of specimens subjected to three-point bending. All specimens initially exhibit a linear response up to approximately 400–500 kN, corresponding to the elastic behavior of the composite section. Beyond this range, a nonlinear response emerges, indicating the onset structural steel and reinforcement yielding, and the extension of matrix cracking and crushing.

Post-yielding, most curves display either a plateau or a gradual increase in load capacity, suggesting strain hardening or redistribution of internal stresses facilitated by the reinforcement and embedded steel section. Distinct load drops followed by partial recoveries are observed in several specimens, indicative of localized cracking, fiber pull-out, or debonding, typical features in fiber-reinforced or ductile composite systems undergoing progressive damage [22], [23]. This type of damage generates a small release of mechanical energy stored in both the specimen and the loading frame. In such cases, both the specimen and the frame tend to slightly unload during tests conducted in position control. Note that in the load-displacement plots presented in the paper —such as Fig. 8— the displacement measurement reflects the reading from the LVDT using the strong floor as a reference. Consequently, the curve also illustrates the snap-back of the loading point during these load drops.

The peak load recorded across specimens ranges from approximately 600 kN to 730 kN, with notable variability. Most specimens retain significant residual load-bearing capacity beyond the peak, demonstrating favorable post-peak ductility. The average ultimate load capacities recorded for beams in sagging and hogging configurations are 719.2 kN and 664.3 kN, respectively.

Beams 3 and 6, tested in sagging and hogging configurations, respectively, were subjected to several steps of sustained loading, and present a reduction of ultimate load capacity by 2.4% and 2.0% in sagging and hogging, respectively, compared to the averages. We are uncertain about the causal relationship between the two phenomena; however, we believe the creep experienced by the fiber-reinforced concrete during the sustained loading may influence subsequent behavior.

The stepwise load drops observed beyond peak loading are attributed to the rupture of longitudinal steel rebars within the reinforcement cage, co-embedded with the steel section. These drops are more significant than previous ones and happen after the maximum load has been reached. They indicate a release of energy and a subsequent increase in stress on other elements, such as the steel profile and fiber-reinforced concrete. These rupture events were corroborated by audible cracking sounds synchronized with abrupt load reductions, confirming progressive failure of individual rebars. The load–displacement curves cluster into two distinct groups, as highlighted in Fig. 8: specimens in the sagging configuration consistently exhibit higher average ultimate loads (713.4 kN) compared to those in the hogging configuration (660.4 kN).

The ductility of the beams tested in the sagging configuration was consistently higher than that of those tested in the hogging configuration. Ductility was quantified using the displacement ductility ratio, as defined by Park et al. [24], which is expressed as the ratio of ultimate displacement ($d_u$) to yield displacement ($d_y$). This ratio serves as an indicator of the beam's capacity for inelastic deformation beyond initial yielding.

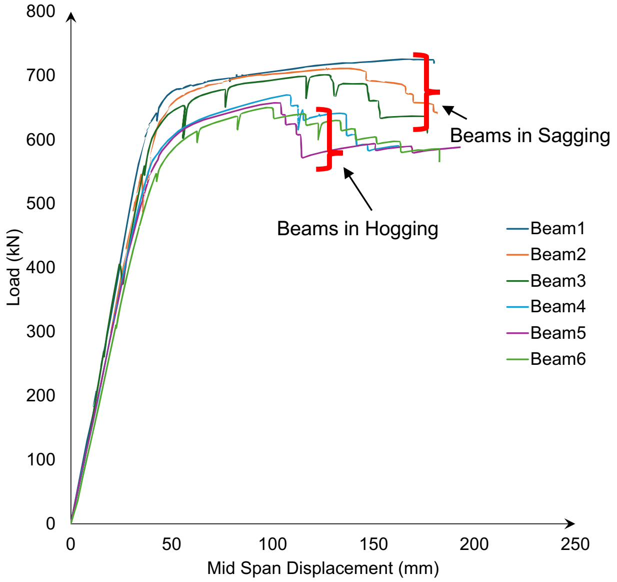

Figure 8. Load–displacement responses of all tested specimens under monotonic loading.

In the present study, the yield displacement ($d_y$) was identified on the ascending branch of the load–displacement curve as the displacement corresponding to 90% of the peak load, occurring just before the maximum load was reached. The ultimate displacement ($d_u$) was determined on the descending branch of the curve, where the load reduced to 90% of the peak load following the maximum point. While Park et al. [24] originally proposed the use of the 80% load level to define ultimate displacement, a 90% criterion was adopted in this work. This modification was necessary because not all tests extended far enough to observe a drop to 80% of the peak load. Despite this adjustment, the 90% threshold provides a consistent and objective basis to evaluate post-peak ductility, especially under the constraint of incomplete post-peak data. A schematic illustration of the ductility measurement methodology is presented in Fig. 9.

Given that the load–displacement responses were nearly identical for the two specimens tested in each configuration, a single representative beam was selected from the sagging and hogging groups for ductility calculation. This allowed for a clear comparison of ductility ratios across configurations. Additionally, these values were compared with the ductility ratio of a beam subjected to sustained loading to assess the effect of loading history on deformation capacity. The results indicate that sustained loading led to a modest reduction in both maximum load and displacement at failure, suggesting some degradation in inelastic deformation capacity over time. However, the overall trend of higher ductility in sagging beams was maintained, potentially due to the favorable stress distribution and confinement conditions offered by the reinforcement layout in this configuration.

As evident from Table 4, the ductility factors are consistently higher for beams tested in the sagging configuration compared to those in the hogging configuration. Although the beam subjected to sustained loading does not exhibit a significant reduction in ductility factor, the corresponding load–displacement response indicates that beams tested under purely monotonic loading demonstrate greater absolute deformation capacity. This suggests that sustained loading may have a subtle effect on post-yield deformation, even if not fully captured by the ductility index alone.

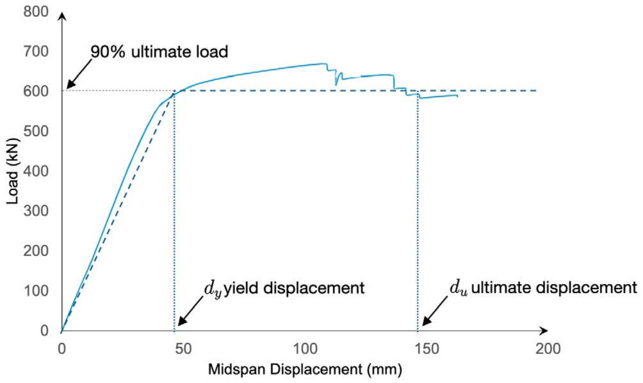

Figure 9. Illustration of ductility calculation based on the structural response curve.

**TABLE 4.**
**Ductility ratios calculated for different beam types.**

| *Specimen* | $d_u/d_y$ |
|---|---|
| Beam 2 (sagging) | 3.88 |
| Beam 3 (sagging, sustained loading) | 3.83 |
| Beam 4 (hogging) | 2.79 |
| Beam 6 (hogging, sustained loading) | 2.78 |

### 3.2. *Evolution of strain contours and crack trajectories*

For Beam 1, the longitudinal strain contours ($\epsilon_{xx}$) presented in Fig. 10 illustrate the evolution and propagation of cracks throughout the loading process. Immediately after crack nucleation, a brief reduction in tensile strain was observed, indicating localized stress relaxation. However, this strain quickly recovered due to the bridging action of the fibers, which effectively transferred stresses across the crack plane. Crack initiation events were accompanied by slight load drops; however, these were minimal and not clearly discernible in the global load–displacement curve. For instance, during stage 2, the initiation of a second crack caused a minor load drop of only 0.14 kN, underscoring the efficiency of the fibers in controlling crack growth and redistributing stresses.

Crack initiation and propagation occurred at an early stage within the linear elastic portion of the load response. The localized strain concentrations observed during these initial stages gradually widened as loading continued, leading to further crack development. Multiple fine cracks formed along the span and gradually opened until failure, demonstrating a distributed cracking mechanism instead of the formation of a single dominant crack. At the yielding stage, as shown in Fig. 10, DIC measurements indicate a strain of 1.0% in compression; however, the specimen remained intact without any visible spalling.

For Beam 2, the longitudinal strain contour plots presented in Fig. 11 reveal that multiple cracks formed at an even earlier stage compared to Beam 1. The overall cracking behavior and mechanisms observed in Beam 1 remain largely applicable here, including the influence of fibers in bridging cracks and redistributing stresses. However, a key observation for Beam 2 is that the material began to show signs of heavy crushing at a strain level of approximately 0.013. Despite this localized deterioration, no visible spalling was observed, and the beam maintained its structural integrity until ultimate failure.

This distinct load drop in Beam 2 response corresponds to localized crushing or deformation within the concrete compression zone shown in Fig. 12. Despite this damage, the presence of fibers ensures that the material remains cohesive, effectively acting as a cushioning layer that transfers loads to the steel beam at the bottom. The load decreases from 547.8 kN to 486.5 kN, representing a significant drop of 61.2 kN. Notably, following this initial load drop, the stiffness of the beam remains relatively stable, indicating that the fibers continue to bridge cracks effectively and preserve the overall structural integrity.

Beam 3, as illustrated in Fig. 13, shows the crack evolution under sagging conditions while being subjected to several steps of sustained loading, as described Section 2. The crack propagation and development closely resemble those observed in Beam 2. However, due to one of the sustained loading steps, a drop of approximately 2.4% is noted compared to the average load capacity of beams tested under static conditions in the sagging configuration. Crack initiation occurs early in the loading process, as depicted in Fig. 13, consistent with the behavior observed in Beams 1 and 2.

It is important to analyze the strain contours during the sustained loading period to better understand its effects on the beam under sagging conditions. Figure 14 presents strain contours at two distinct stages of sustained loading, highlighting a slight reduction in strain levels that corresponds with relaxation phenomena and a concurrent decrease in load val-

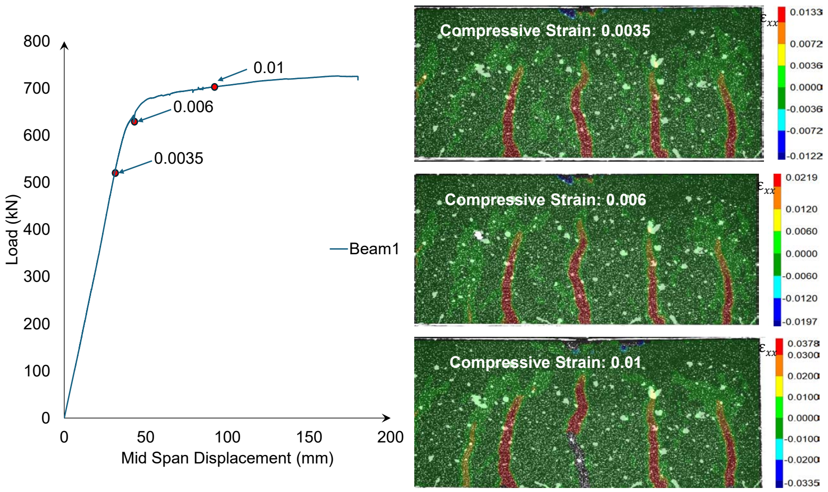

Figure 10. Longitudinal strain contour plots for Beam 1 at various loading stages, illustrating early multiple crack formation.

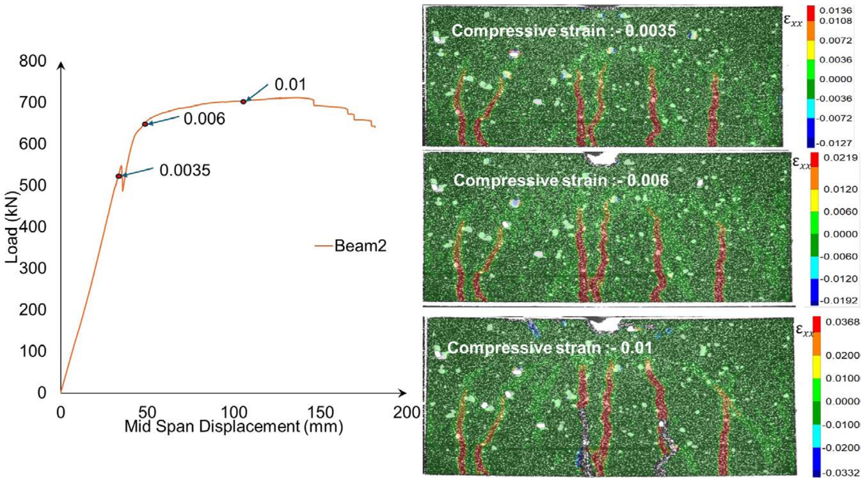

Figure 11. Longitudinal strain contour plots for Beam 2 at various loading stages, illustrating early multiple crack formation.

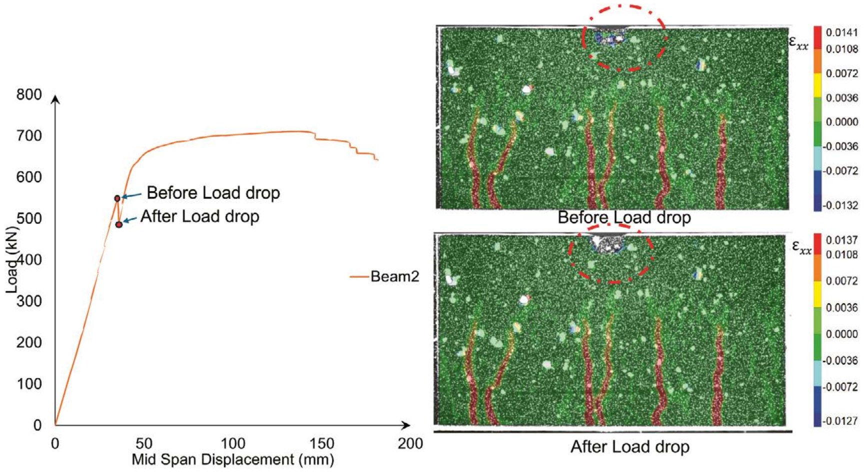

Figure 12. Longitudinal strain contour plots for Beam 2 before and after load drop.

ues. DIC analysis reveals that during this relaxation phase, crack depth increases notably by 7.8 mm, particularly at one dominant crack accompanied by branching as shown in Fig. 14. This crack progression is accompanied by a relaxation in the load response, which impacts the overall load-carrying capacity of the beam. At the onset of sustained loading, the beam carries a load of 271.4 kN, which decreases to 260.8 kN by the end of the 20-minute period. Additionally, crack branching was observed during the sustained load, indicating continued microstructural changes despite the reduced load.

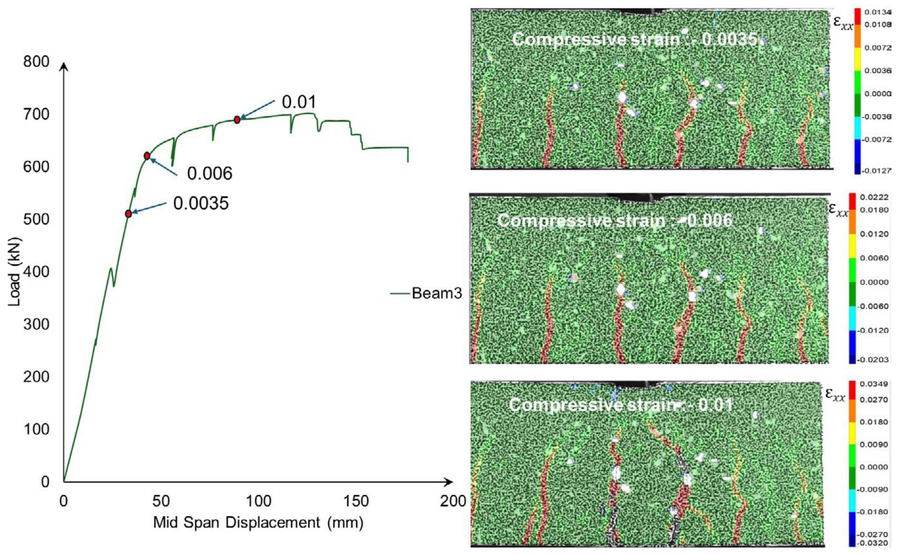

Figure 13. Longitudinal strain contour plots for Beam 3 at various loading stages, illustrating early multiple crack formation.

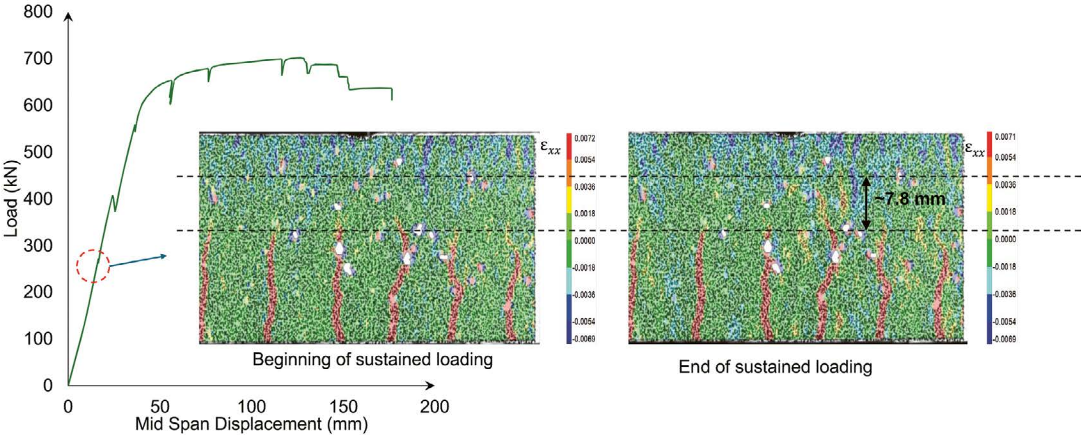

Figure 14. Longitudinal strain contour plots for Beam 3 before and after sustained loading at approximately 40% of the load peak.

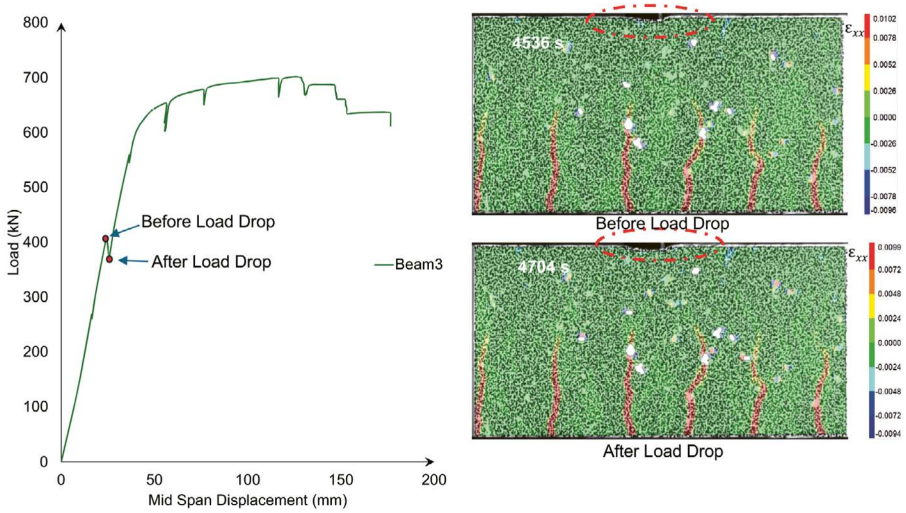

Figure 14. Longitudinal strain contour plots for Beam 3 before and after sustained loading at approximately 40% of the load peak.

Similarly, a noticeable load drop occurs in the initial stage of Beam 3's load response, akin to the behavior observed in Beam 2. Following this initial load drop, the stiffness of the beam remains largely unchanged, as reflected in the load response shown in Fig. 15. The load decreases from 407.2 kN to 372.4 kN, a total drop of 34.8 kN. Although no new crack

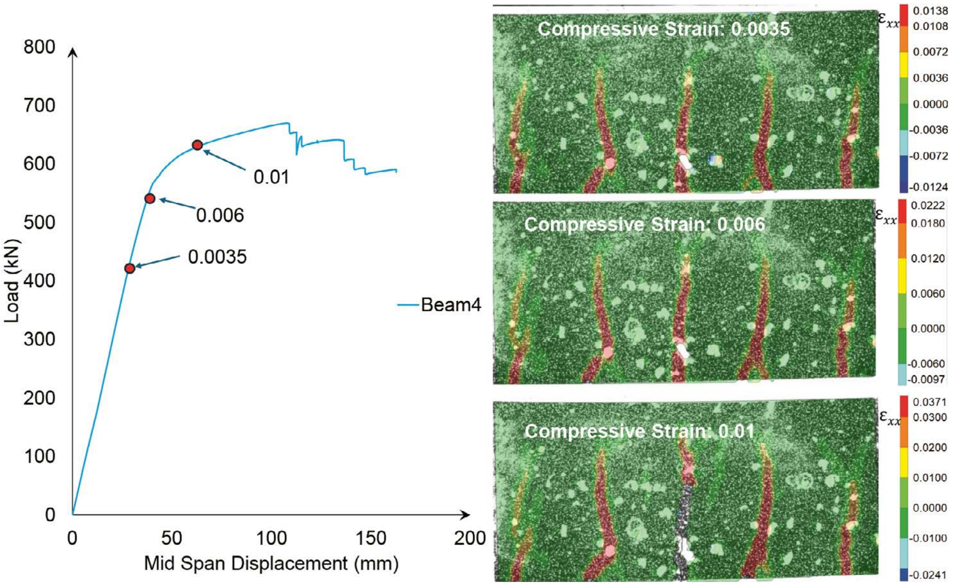

Figure 16. Longitudinal strain contour plots for Beam 4 (hogging) at various loading stages, illustrating early multiple crack formation.

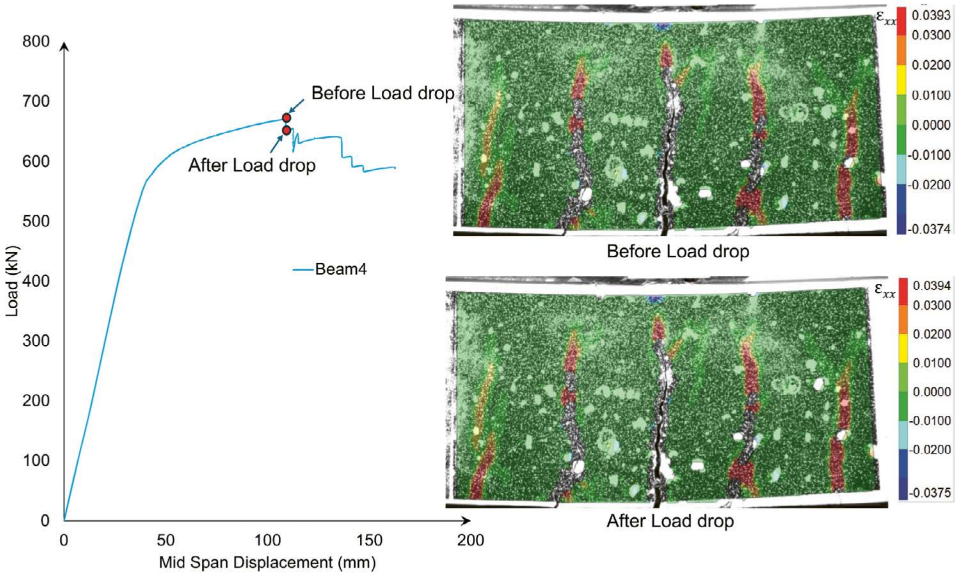

Figure 17. Longitudinal strain contour plots for Beam 4 (hogging) explaining the cause of the intermediate load drop that it experiences.

formation was detected through DIC analysis, some strain redistribution was observed.

From the response of Beam 4 shown in Fig. 16, it is evident that under hogging conditions crack initiation, as well as the formation of multiple cracks, occurs much earlier in the load response compared to the sagging configuration. Similar to what was observed in the sagging tests, the cracks that developed at the very beginning of loading continued to propagate and widen as the load increased, demonstrating a consistent cracking mechanism despite the different bending configuration.

The load drop in Beam 4 occurs only after the load response enters the nonlinear region and begins to plateau, as shown in Fig. 17. While no new cracks are observed during this stage, the sudden reduction in load can be attributed to localized debonding within the concrete matrix. This debonding is subsequently mitigated by the fibers, which bridge the cracks and help redistribute stresses, allowing the beam to maintain its structural integrity despite the loss in load capacity. One of the observations is that the load drop occurs at the ultimate load value in the case of hogging configuration in beams without sustained load.

The crack evolution and propagation in Beam 5, as illustrated in Fig. 18, closely mirror the behavior observed in Beam 4. Similar to Beam 4, crack formation in Beam 5 occurs at a very early stage of the load response, even while the response remains within the linear range. This early cracking pattern suggests that, under similar loading conditions, the hogging configuration promotes quicker crack initiation before the onset of significant nonlinear behavior.

Figure 19 presents the strain contours for Beam 6, where the pattern of crack initiation and propagation is largely consistent with the behaviors observed in Beams 4 and 5. The cracks form early in the loading process and progress in a

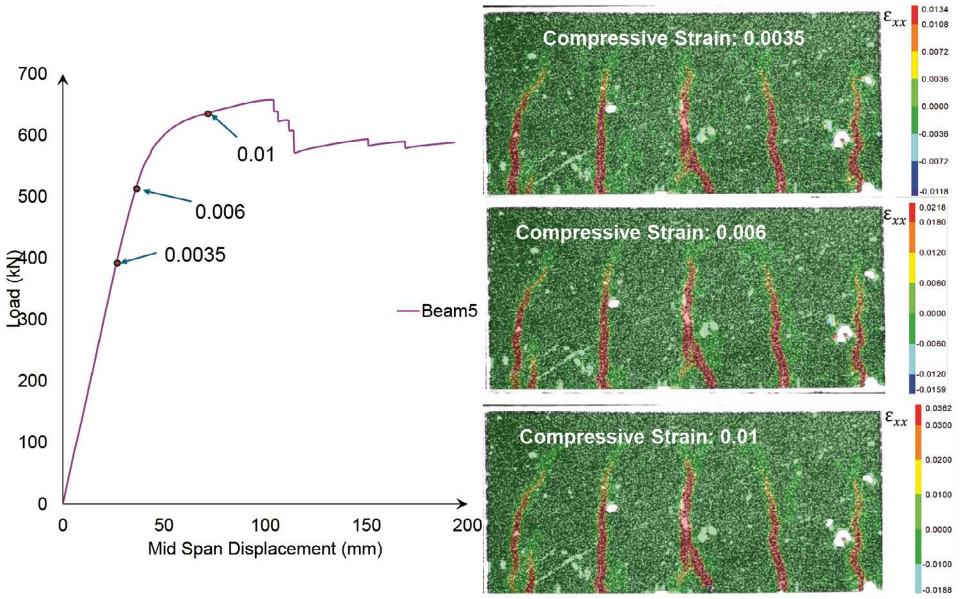

Figure 18. Longitudinal strain contour plots for Beam 5 (hogging) at various loading stages, illustrating early multiple crack formation.

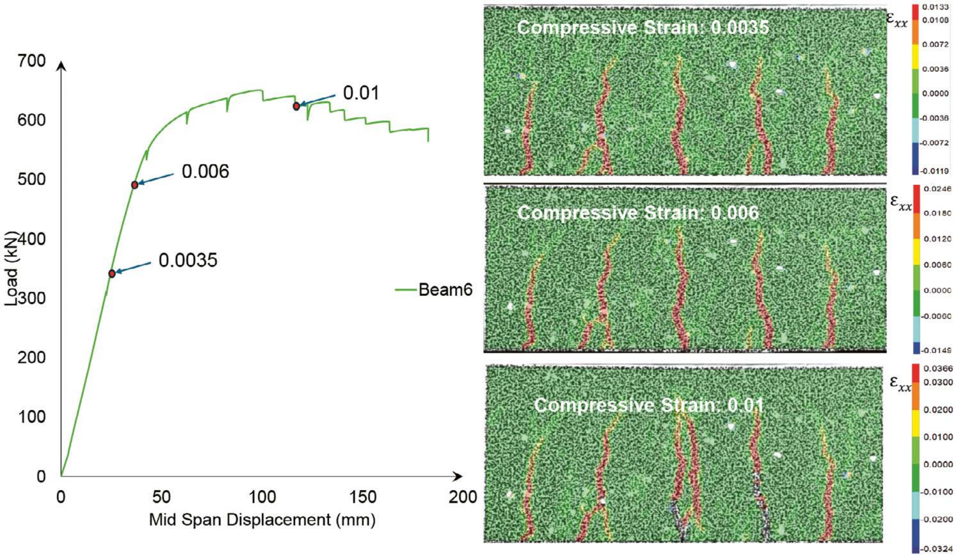

Figure 19. Longitudinal strain contour plots for Beam 6 (hogging) at various loading stages, illustrating early multiple crack formation.

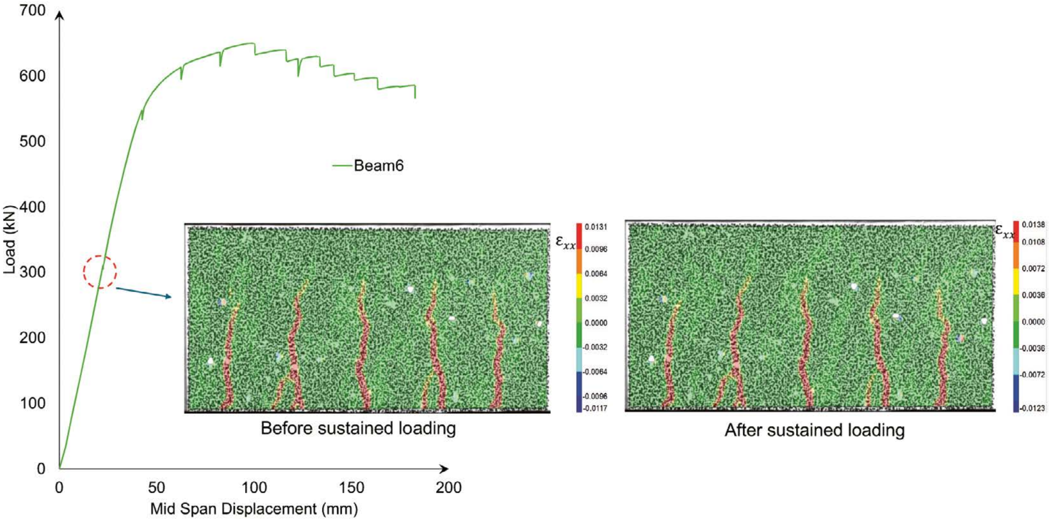

Figure 20. Longitudinal strain contour plots for Beam 6 (hogging) before and after sustained loading at approximately 40% of the load peak.

comparable manner, indicating a similar structural response under the given hogging configuration.

In the case of beams tested under hogging conditions, the concrete in the compression zone experiences very high strains, exceeding 1%, yet it remains intact without the crushing observed in beams tested in the sagging configuration. Before and after the sustained loading steps, no significant changes are observed in the crack patterns or their propagation in the hogging tests. However, both compressive and tensile strain levels show a slight increase, which can be attributed to creep effects during the sustained loading phases (see Fig. 20).

The load response of beams in the hogging configuration does not exhibit the distinct load drop observed in the sagging beams; instead, a gradual hardening behavior is evident. DIC analysis clarifies that the sharp load drop seen in the sagging case is linked to deformation of the concrete in the compressive zone directly beneath the point load. In contrast, under hogging conditions, the load transfer is primarily facilitated through the steel section, preventing localized crushing and contributing to the smoother, hardening-type response observed in these beams.

At an average strain level close to 0.013, the material in the compressive zone of the sagging beams begins to crush. Even though the concrete undergoes crushing, as shown in the final stage (Figs. 12 and 15), the presence of fiber reinforcement ensures that the crushed concrete behaves like a packing material, continuing to transfer load to the steel section. In contrast, in the hogging configuration, the beam maintains its structural integrity even at much higher compressive strain levels, reaching up to 4.14%, demonstrating the combined effectiveness of the fibers and the steel section.

### 3.3. *Evolution of compressive strains in the concrete compression zone throughout the load response.*

As mentioned in the introduction, the HTC used in these beam specimens has been shown to withstand exceptionally high levels of compressive strain. The addition of steel fibers improves the ductility of the concrete, enabling it to endure significantly greater strains compared to conventional mixes. Therefore, studying the evolution of compressive strain during the loading process is particularly important, as it provides experimental validation for the enhanced strain capacity of HTC, as previously reported by Ruiz et al. [9].

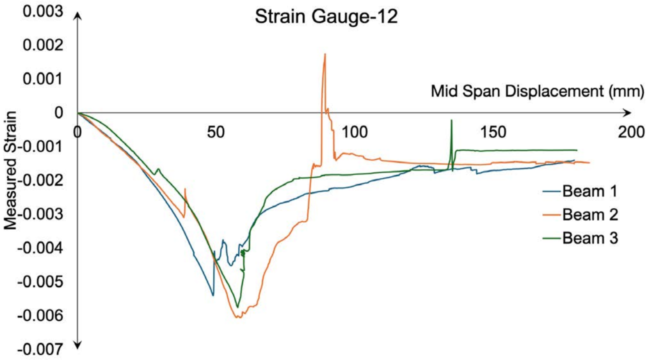

Figure 21. Recordings by the top strain gauge in compression.

Figure 21 shows the recordings of the top strain gauge in compression of all the beams tested in sagging. All the beams reach very high levels of compressive strain, way higher than what is usual for concrete structures, which have a limit of 0.35%, reaching roughly the 0.6% allowed in the Ultimate Limit State (ULS) by Annex L of the new Eurocode 2 [10]. The three beams consistently align with the readings taken via DIC, as shown in Figs. 10-13. However, the deformation and bending just below the actuator prevented the strain gauges from functioning properly beyond 0.6%. In spite of this, DIC measurements confirm that all the beams reach 1% compressive strain with no signs of crushing. Eventually, signs of crushing appear, but the fibers keep the concrete in place until the end of the tests.

In the hogging tests, the strain gauges failed to provide reliable measurements due to early cracking and concentrated rotation. However, the DIC results shown in Figs. 16-19 indicate that the levels of ductility in compression were similar to those in sagging.

### 3.4. *Crack mouth opening calculations*

Crack widths were calculated from displacement profiles by analyzing a selected section x–x, shown in Fig. 22, located at the bottom of the beam. The displacement profile was asymptotically matched on either side of the crack, and the crack opening was determined by subtracting the displacements immediately adjacent to the crack on the left and right sides.

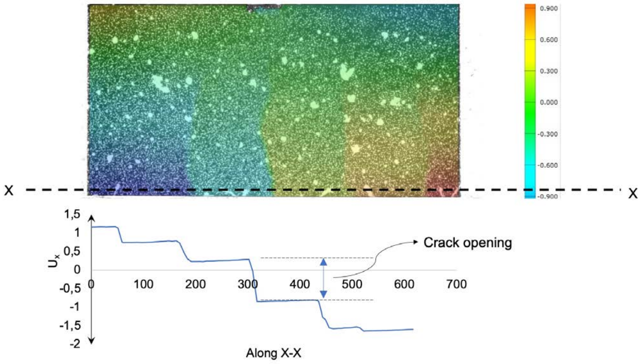

Figure 22. Displacement-based calculation of crack width at section x–x located at the beam bottom surface.

Figure 23 compares CMOD time histories obtained from DIC gauges placed across the crack mouth for four of the beams, grouped by bending regime (sagging left, hogging right) and by stage (monotonic loading up, relaxation down). In sagging at monotonic loading (Beam 1), several cracks open gradually at a similar slow rate until the hinge below the loading point forms, which coincides approximately with the initiation of the second loading ramp. Then the opening rate speeds up, and, eventually, there is a crack (marked as 2) that starts to localize most of the opening so that the rest of the nearby cracks (1 and 3) tend to close. Beam 4, tested in hogging at monotonic loading, behaves similarly, but the openings are higher, and the localization in crack 2 is more abrupt.

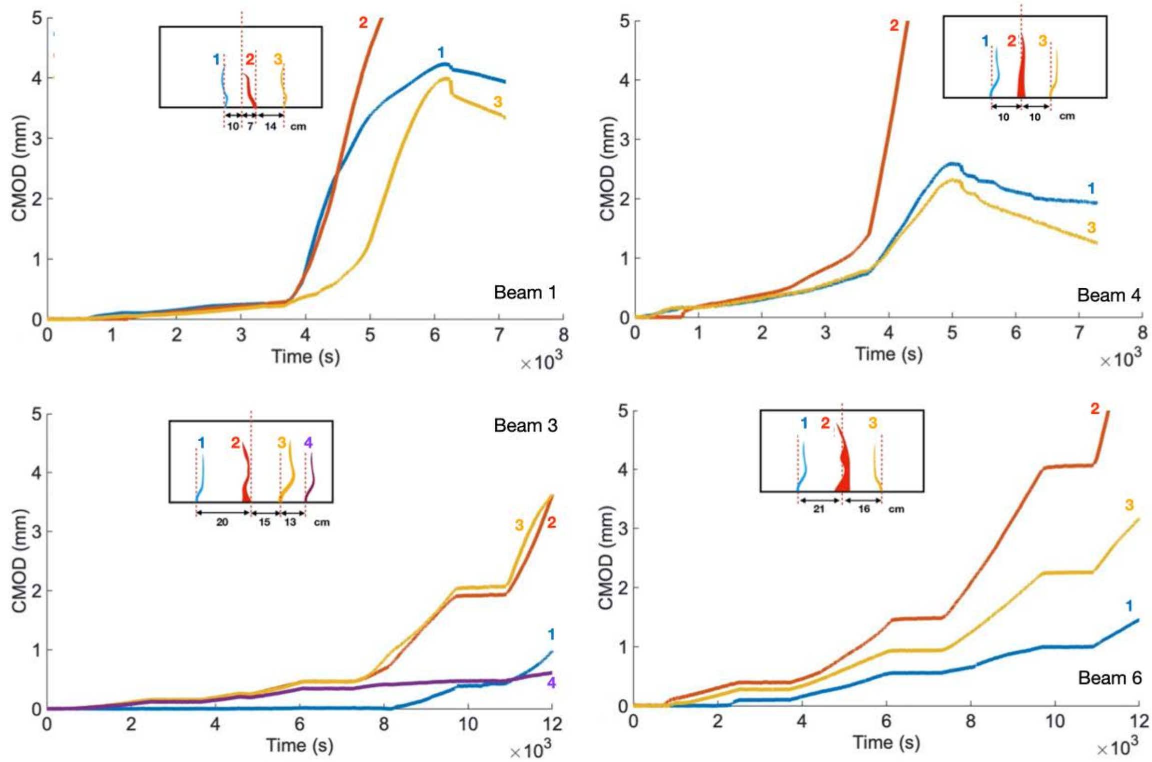

Figure 23. Comparison of CMOD development across sagging and hogging configurations in monotonic and relaxation loading.

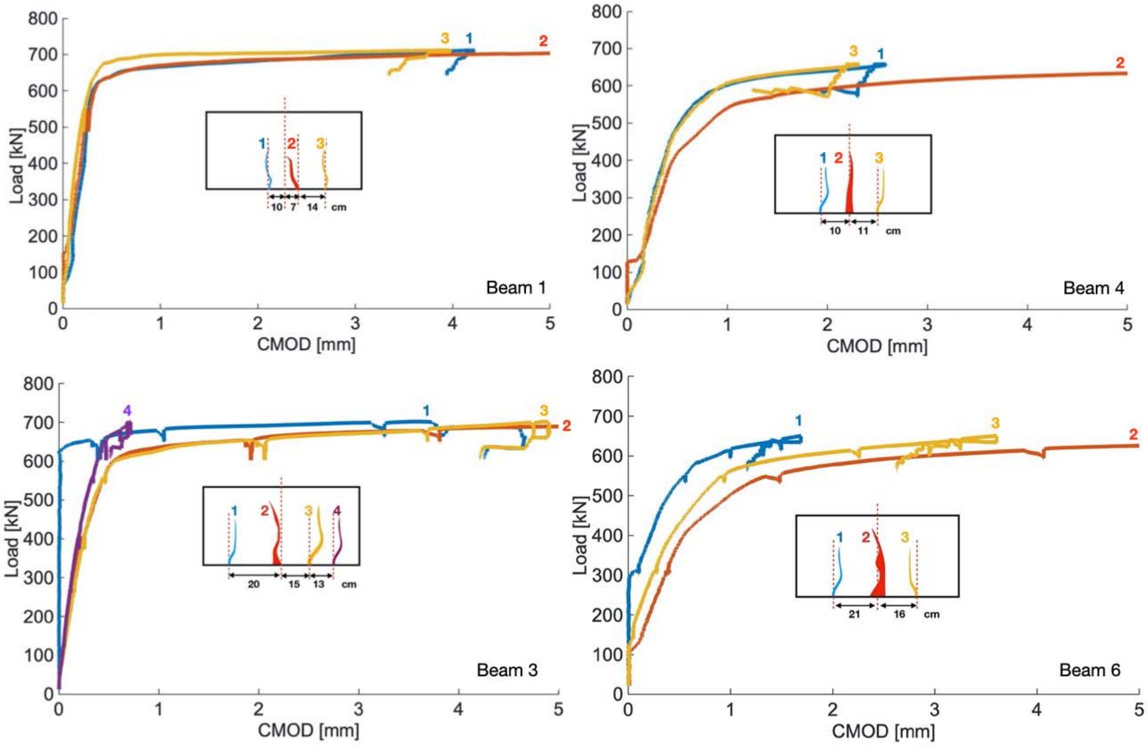

Figure 24. Comparison of Load-CMOD development across sagging and hogging configurations in monotonic and relaxation loading.

The lower line of subfigures in Fig. 23 presents the CMOD histories for two beams subjected to sustained loading. Beam 3, which is sagging, exhibits very slow crack growth during the periods of sustained load. However, it appears that the crack opening rate increases after the application of the same nearly constant displacement rate applied before the relaxation stage (5 mm/min). We believe this may be due to a slight progressive damage or creep at the matrix-fiber interface during the sustained stage. Similarly, Beam 6 shows a comparable behavior, but with higher openings and rates. This is likely a result of the beam's section configuration, which places greater demands on the SFRC in the tensioned fibers.

Figure 24 shows the load-CMOD curves for the same beams and cracks as in Fig. 23. The curves of Beam 1 show that the openings are below 0.5 mm during the linear ramp-up, but start to grow significantly once the steel profile starts yielding. Eventually, all the opening localizes in crack 2, while the other studied cracks, 1 and 3, stall and even begin to close. Beam 4 follows the same trend as Beam 1, but shows wider openings and earlier localization in the central crack.

The load-CMOD plots for beams undergoing relaxation steps are displayed in the lower row of subfigures in Fig. 24. It is evident that the crack openings in these beams are wider compared to those in the beams that were subjected to monotonous loading. As mentioned above, this observation suggests a slight deterioration or creep at the matrix-fiber interface.

Table 5 presents the critical CMODs —at failure— ($w_{Mc}$) for the six beams tested. In the case of hogging, the critical crack opening is much larger than in sagging because of the absence of the steel section near the tensile fibers of the beam.

In the case of hogging, where the steel section is located at the top of the beam, a single-section failure is observed. Although multiple cracks may appear, only one section ultimately opens up until failure occurs. In contrast, when sagging takes place, the beam experiences widespread cracking. In all instances, there is one crack that becomes significantly larger than the others, ultimately leading to the failure of the beams.

In nearly all cases, the crack pattern remains largely unchanged, with no significant new crack initiations occurring beyond the initial portion of the load response, at least within the range captured by the DIC camera.

**TABLE 5.**
**Critical crack openings at failure.**

| *Specimen* | *$w_{Mc}$ [mm]* |
|---|---|
| Beam 1 (sagging) | 10.20 |
| Beam 2 (sagging) | 16.87 |
| Beam 3 (sagging) | 21.15 |
| Beam 4 (hogging) | 30.08 |
| Beam 5 (hogging) | 40.99 |
| Beam 6 (hogging) | 42.10 |

### 3.5. *Crack Spacing Measurement Results*

Crack spacing was assessed using a combination of manual measurements and DIC post-processing. Figure 25 illustrates the schematic representation of the DIC region at midspan, highlighting how cracks were identified and inter-crack spacing was measured. The primary area of interest covered a 660 mm segment centered at midspan, which corresponds to the zone of maximum bending moment and was captured using DIC. Within this area, cracks were identified based on distinct separation lines in the displacement contour maps. The analysis included both major cracks and smaller microcracks that fell within the spatial resolution of the DIC system. For cracks located outside the DIC field of view, visual inspection and photographic documentation were used for manual mapping along the remaining beam length. Crack spacing was then calculated as the distance between successive cracks along the entire span, allowing for a comprehensive evaluation of crack distribution in both sagging and hogging configurations.

Each beam was segmented into four equal-length zones (0–110 cm, 110–220 cm, 220–330 cm, and 330–440 cm), and the number of visible cracks in each zone was recorded. Table 6 summarizes the total number of cracks and average spacing for six beams. Sagging beams (Beams 1–3) exhibited a more distributed cracking pattern, with an average spacing of approximately 12.9 cm, while hogging beams (Beams 4, 6, 7) showed slightly wider spacing, indicating a more localized cracking response.

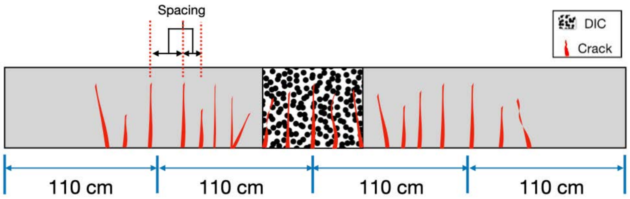

Figure 25. Schematic of crack spacing measurement zone showing DIC region and crack tip identification.

**TABLE 6.**
**Total number of cracks and average spacing.**

| *Specimen* | *Number of cracks* | *Avg. Spacing [cm]* |
|---|---|---|
| Beam 1 (sagging) | 20 | 12.90 |
| Beam 2 (sagging) | 21 | 12.95 |
| Beam 3 (sagging) | 9 | 12.84 |
| Beam 4 (hogging) | 24 | 10.11 |
| Beam 6 (hogging) | 15 | 14.46 |
| Beam 7 (hogging) | 18 | 14.00 |

To analyze the spatial distribution of cracking, Table 7 presents the number of cracks observed in each beam zone. In sagging specimens, cracks were more uniformly distributed across the central zones (Mid-Left and Mid-Right), suggesting effective strain redistribution through fiber bridging. In contrast, hogging beams exhibited pronounced clustering of cracks near midspan.

**TABLE 7.**
**Zone-wise crack distribution across beam span.**

| *Specimen* | *Left 0–110 cm* | *Mid-Left 110–220 cm* | *Mid-Right 220–330 cm* | *Right 330–440 cm* |
|---|---|---|---|---|
| Beam 1 | 1 | 8 | 9 | 1 |
| Beam 2 | 1 | 9 | 10 | 1 |
| Beam 3 | 0 | 3 | 6 | 0 |
| Beam 4 | 3 | 11 | 9 | 1 |
| Beam 6 | 0 | 9 | 6 | 0 |
| Beam 7 | 2 | 8 | 8 | 0 |

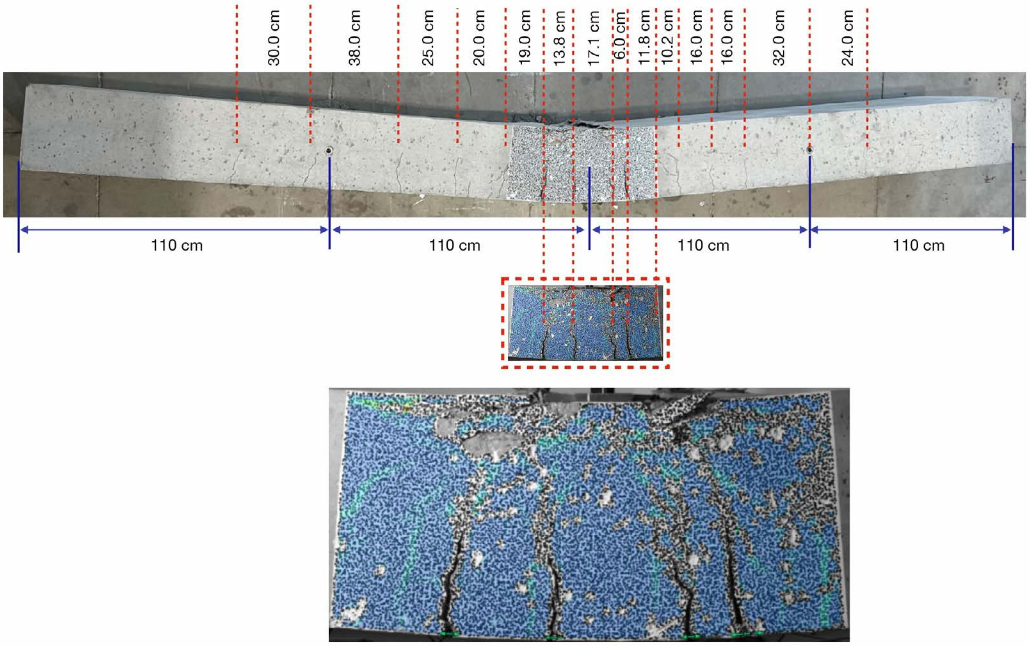

Figure 26. Crack spacing analysis for Beam 2 (Sagging configuration).

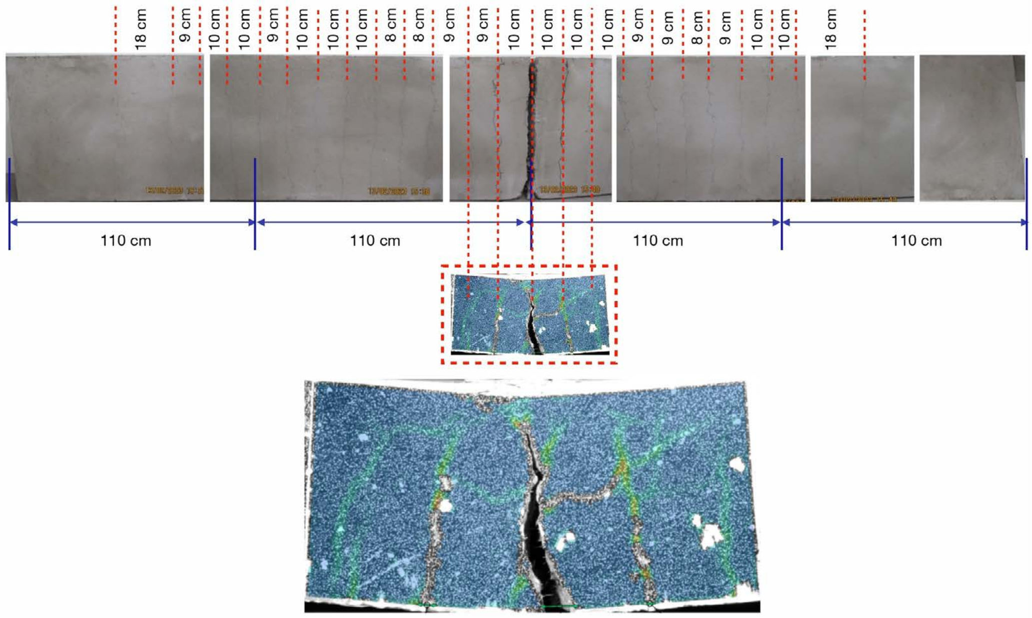

Figure 27. Crack spacing analysis for Beam 4 (Hogging configuration).

Figures 26 and 27 illustrate annotated crack maps obtained from DIC analysis for Beam 2 (sagging) and Beam 4 (hogging), respectively. The sagging configuration shows evenly distributed cracks across the midspan region, while the hogging case displays fewer but more dominant cracks forming closer to midspan.

Overall, the observed differences in crack spacing reflect the role of structural configuration and fiber contribution. Sagging beams, with the steel section located in tension, promote distributed cracking and effective fiber engagement. Conversely, hogging beams develop dominant cracks due to the higher contribution of SFRC in the tension zone, which cannot be redistributed to other cracks once a given crack reaches the decreasing point where fibers are pulled out.

## 4.
## DISCUSSION

The results obtained from the full-field DIC monitoring of SFRC–steel composite beams highlight several critical aspects of fracture behavior under static and sustained loading. In both sagging and hogging configurations, early crack initiation was observed within the serviceability load range where the structural behavior is approximately linear, with cracks progressively widening as loading continued. The distributed crack patterns in sagging beams, promoted by the tensile positioning of the steel section and enhanced fiber bridging, contrast with the more localized cracking observed in hogging specimens. This distinction is consistent with strain redistribution behavior and the availability of confinement near the tension zone.

The application of several steps of sustained loading introduced moderate changes in behavior, particularly in sagging beams. The overall reduction in peak load was limited (2–3%) and nonconclusive. DIC results revealed strain redistribution, increased crack depth (up to 7.8 mm) and opening rate, and branching phenomena not captured by conventional LVDTs. In contrast, hogging beams exhibited minimal change in crack patterns during sustained loading, but showed incremental increases in tensile and compressive strain values due to creep.

Compressive strain development shows the superior ductility of the HTC used in the study. All of the beams reached a 1% compressive strain with no visible crushing. Strain levels exceeding 1% were maintained in sagging specimens, although signs of matrix crushing appeared beyond this threshold. Despite the material being crushed, it continued to resist compression because of the fibers, and there was no spall failure in any case. Meanwhile, hogging beams withstood compressive strains well above 1% without visible crushing or spalling, thanks to the contribution of the stiff steel section located in compression. These observations align with prior reports on HTC and confirm its ability to endure large strains without brittle failure.

By allowing these higher strains, it is possible to optimize the materials' performance in composite structures. Specifically, this approach allows for the full utilization of the structural steel at ULS, as noted in previous papers [8], [9], [16]. Additionally, composite structural elements that leverage the significant ductility of SFRC in compression can reduce the carbon footprint by up to 40% when compared to alternative structural concrete solutions for the same structure, as demonstrated by some of the authors [25].

Annex L of the new Eurocode 2 [10] states that the maximum strain in any structural element made from SFRC is 0.6% under the ULS, compared to 0.35% for standard concrete. Additionally, the compressive model in Annex L shows that the SFRC used in our research, with compressive and flexural classes of C45/55 and 2.5c, respectively, can reach a strain of 0.89% in the Serviceability Limit State (SLS) [9]. Here, we demonstrate that these strain levels can be surpassed while the beams remain fully functional. Moreover, the beams examined in this paper achieve very high levels of compressive strain without any spalling in the top layer. These results confirm the material's reliability even under extreme loading conditions. Therefore, our study experimentally validates the principles outlined in Annex L at the structural level.

CMOD results further confirmed the structural distinction between configurations. Sagging beams displayed lower critical crack openings (10–21 mm) and distributed fracture mechanisms, whereas hogging beams reached crack openings up to 42 mm due to the lack of strain hardening in the tensile region. This behavior confirms the critical role of steel profile positioning in influencing crack propagation modes.

Moreover, the insights into crack development patterns and spacing gained during the campaign directly influence the design of composite beams and can help refine standard specifications on these topics. By understanding where and how cracks initiate and propagate in composite SFRC-structural steel structures, it is possible to optimize material placement and fiber reinforcement strategies to enhance durability and performance. This knowledge enables practical design adjustments that improve stress management.

Overall, the use of DIC in this experimental setup was highly effective for monitoring strain localization, crack spacing, and CMOD with excellent spatial and temporal resolution. Compared to traditional instrumentation, DIC offered valuable insights into strain redistribution, early microcracking, and crushing phenomena. However, there are challenges that need to be addressed in future studies, including the quality of the speckle pattern, uniformity of lighting, and limited coverage of the field of view. These issues could potentially be resolved by expanding to 3D-DIC or using synchronized multi-camera systems.

## 5.
## CONCLUSIONS

This experimental study investigated the fracture response of full-scale SFRC–steel composite beams under monotonic and sustained loading using a standard extensometry and a DIC system. The following conclusions can be drawn:

- *Strain Localization and Cracking*: DIC effectively captured early crack initiation, branching, and propagation. Sagging beams exhibited distributed cracking due to favorable tensile reinforcement conditions, while hogging beams displayed dominant, localized cracks.
- *CMOD and Crack Morphology*: CMOD values at failure ranged from 10 mm in sagging to over 40 mm in hogging beams. The presence of the steel section in tension promoted strain hardening and ductile behavior in sagging beams, while its position in compression in hogging beams limited tensile redistribution.
- *Compressive Strain Capacity*: The high-performance HTC matrix accommodated compressive strains well above 1% in sagging and hogging configurations without catastrophic failure, demonstrating enhanced ductility and compatibility with fiber-reinforced design models.
- *Sustained Loading Effects*: DIC revealed microstructural changes such as crack branching and increased crack depth, which were not evident through conventional instrumentation. Besides, CMOD histories reveal that the opening rate increases after a period of sustained loading, which could be attributable to deterioration or creep of the matrix-fiber interface.
- *Eurocode 2 Annex L Validation*: The experimental results confirm the applicability of Annex L residual strength-based compressive model and related strain limits in compression to full-scale SFRC composite beams. The strain and cracking behavior align well with design assumptions, supporting broader adoption in structural applications.
- *DIC as a Structural Monitoring Tool*: This study confirms the robustness and practicality of DIC in large-scale testing of composite beams. It offers a powerful complement to traditional sensors and paves the way for its inclusion in future monitoring guidelines and standards.

Future work should focus on exploring cyclic and fatigue behavior under varying load regimes, expanding to 3D-DIC setups, and validating numerical models for further generalization of these findings in the design and assessment of hybrid SFRC structures.

## *Acknowledgements*

ArcelorMittal Global R&D. provided the funding for the tests. Additionally, this research received financial support from the *Ministerio de Innovación, Ciencia y Universidades* in Spain through grant PID2023-147971OB-C31, from the *Junta de Comunidades de Castilla-La Mancha* in Spain via grant SBPLY/24/180225/000003, and from the *Universidad de Castilla-La Mancha* and the ERDF through grant 2025-GRIN-38445.

## *Dedication*

The authors dedicate this work to Professors Hugo Corres and Toni Marí in celebration of their seventieth anniversary and their remarkable, inspiring careers. In particular, Gonzalo Ruiz expresses heartfelt gratitude to Toni Marí for the many stimulating discussions on the applications of fracture mechanics to concrete technology, as well as for his kindness and friendship.

## *References*

[1] B. Lai, J. Y. R. Liew, and A. L. Hoang, "Behavior of high strength concrete encased steel composite stub columns with C130 concrete and S690 steel," *Engineering Structures*, vol. 200, p. 109743, 2019, doi: 10.1016/j.engstruct.2019.109743.

[2] J. Zhao, Y. Sang, and F. Duan, "The state of the art of two-dimensional digital image correlation computational method," *Engineering Reports*, vol. 1, no. 8, p. e12038, 2019, doi: 10.1002/eng2.12038.

[3] B. Lai, J. Y. R. Liew, A. Venkateshwaran, S. Li, and M. Xiong, "Assessment of high-strength concrete encased steel composite columns subject to axial compression," *Journal of Constructional Steel Research*, vol. 164, p. 105765, 2020, doi: 10.1016/j.jcsr.2019.105765.

[4] A. Memarzadeh and M. Nematzadeh, "Axial compressive performance of steel reinforced fibrous concrete composite stub columns: Experimental and theoretical study," *Structures*, vol. 34, pp. 2455–2475, 2021, doi: https://doi.org/10.1016/j.istruc.2021.08.130.

[5] S. J. Foster and R. I. Gilbert, "Characterisation and structural design of steel fibre reinforced concrete," *Structural Concrete*, vol. 19, no. 1, pp. 121–132, 2018, doi: 10.1002/suco.201700156.

[6] G. Ruiz, Á. De La Rosa, S. Wolf, and E. Poveda, "Model for the compressive stress-strain relationship of steel fiber-reinforced concrete for non-linear structural analysis," *Hormigón y Acero*, vol. 69(S1), pp. 75–80, 2018, doi: 10.1016/j.hya.2018.10.001.

[7] G. Ruiz, Á. De La Rosa, and E. Poveda, "Relationship between residual flexural strength and compression strength in steel-fiber reinforced concrete within the new Eurocode 2 regulatory framework," *Theoretical and Applied Fracture Mechanics*, vol. 103, p. 102310, 2019, doi: 10.1016/j.tafmec.2019.102310.

[8] R. Zanon, M. Schäfer, G. Ruiz, Á. De La Rosa, and Q. Zhang, "Steel-fibre reinforced concrete in composite structures as a means to increase resistance and ductility," *Stahlbau*, vol. 91, no. 12, pp. 801–811, 2022.

[9] G. Ruiz, Á. De La Rosa, E. Poveda, R. Zanon, M. Schäfer, and S. Wolf, "Compressive behavior of steel-fiber reinforced concrete in Annex L of new Eurocode 2," *Hormigón y Acero*, vol. 74, no. 299–300, pp. 187–198, 2023.

[10] CEN, Eurocode 2, Design of concrete structures. Part 1-1: General rules – Rules for buildings, bridges and civil structures, prEN 1992-1-1: 2022. CEN–European Committee for Standardization, Brussels, Belgium, 2022.

[11] Á. De La Rosa, G. Ruiz, V. W. Masih, and R. Zanon, "Experimental study of the response to fatigue compression and indirect tensile loading in high-technology concrete," *Materials and Structures*, vol. 58, p. 207, 2025, doi: 10.1617/s11527-025-02731-9.

[12] M. Mahal, T. Blanksvärd, B. Täljsten, and G. Sas, "Using digital image correlation to evaluate fatigue behavior of strengthened reinforced concrete beams," *Engineering Structures*, vol. 105, pp. 277–288, 2015, doi: 10.1016/j.engstruct.2015.10.017.

[13] A. Baktheer and H. Becks, "Fracture mechanics based interpretation of the load sequence effect in the flexural fatigue behavior of concrete using digital image correlation," *Construction and Building Materials*, vol. 307, p. 124817, 2021, doi: 10.1016/j.conbuildmat.2021.124817.

[14] R. Janeliukstis and X. Chen, "Review of digital image correlation application to large-scale composite structure testing," *Composite Structures*, vol. 271, p. 114143, 2021, doi: 10.1016/j.compstruct.2021.114143.

[15] J. Holmes, S. Sommacal, R. Das, Z. Stachurski, and P. Compston, "Digital image and volume correlation for deformation and damage characterisation of fibre-reinforced composites: A review," *Composite Structures*, vol. 315, p. 116994, 2023, doi: 10.1016/j.compstruct.2023.116994.

[16] R. Zanon, M. Schäfer, G. Ruiz, Á. De La Rosa, V. W. Masih, and S. Wolf, "Experimental bending tests on encased steel-concrete composite beams with SFRC," in *11th international conference on fibre-reinforced concrete* (BEFIB 2024), Dresden, Germany, 2024. doi: 10.1007/978-3-031-70145-0_25.

[17] CEN, Eurocode 4, Design of composite steel and concrete structures. Part 1-1: General rules and rules for buildings, prEN 1994-1-2: 2022. 2022.

[18] Á. De La Rosa, G. Ruiz, V. M. Masih, and R. Zanon, "Innovative high-technology concrete mix design method integrating rheological properties and fracture mechanics," *Construction and Building Materials*, vol. 458, p. 139538, 2025, doi: 10.1016/j.conbuildmat.2024.139538.

[19] R. Henning, Water-based screenprinting today: Hands-on techniques to digital technology. New York: Watson-Guptill Publications, 2006.

[20] G. Crammond, S. W. Boyd, and J. M. Dulieu-Barton, "Speckle pattern quality assessment for digital image correlation," *Optics and Lasers in Engineering*, vol. 51, no. 12, pp. 1368–1378, 2013, doi: 10.1016/j.optlaseng.2013.03.014.

[21] *GOM GmbH ARAMIS User Manual Hardware*. GOM GmbH: Braunschweig, Germany, 2022.

[22] S. Li, H. Lv, T. Huang, Z. Zhang, J. Yao, and X. Ni, "Degradation of reinforced concrete beams subjected to sustained loading and multi-environmental factors," *Buildings*, vol. 12, no. 9, 2022, doi: 10.3390/buildings12091382.

[23] M. Shubaili, A. Elawadi, S. Orton, and Y. Tian, "Time-dependent behavior of reinforced concrete beams under high sustained loads," *Applied Sciences (Switzerland)*, vol. 12, no. 8, 2022, doi: 10.3390/app12084015.

[24] R. Park, "Ductility evaluation from laboratory and analytical testing," in *Proceedings of the Ninth World Conference on Earthquake Engineering*, 1988.

[25] S. Wolf, G. Ruiz, Á. De La Rosa, E. Poveda, M. Schäfer, and R. Zanon, "Ductility in compression of SFRC and its use with low CO_2 emissions green steel fibres," in Proceedings of FRC2023. Fiber Reinforced Concrete: From Design to Structural Applications. Joint ACI-fib-RILEM International Workshop, Phoenix, Arizona, 2023.